Optical Materials: X 25 (2025) 100382

Contents lists available at ScienceDirect

Optical Materials: X

journal homepage: www.journals.elsevier.com/optical-materials-x

Effect of rhodium doping for photocatalytic activity of barium titanate

G.A. Kaptagay [a], B.M. Satanova [b], A.U. Abuova [b], M. Konuhova [c], Zh.Ye. Zakiyeva [b], U. Zh Tolegen [b], N.O. Koilyk [a], F.U. Abuova [b,*]

[a] Institute of Physics, Mathematics and Digital Technologies, Kazakh National Women's Teacher Training University, Almaty, Kazakhstan
[b] Department of Technical Physics, L.N. Gumilyov Eurasian National University, Astana, Kazakhstan
[c] Institute of Solid State Physics, University of Latvia, Riga, Latvia

ARTICLE INFO

Keywords:
Electrocatalysis
Photocatalysis
Energy storage and conversion
Electrode materials
Water splitting

ABSTRACT

By means of DFT oxygen evolution reaction on Rh-doped $BaTiO_3$ (001) surface has been modeled. Gibbs free energies for each step of the reaction as well as the values of overpotential have been calculated, taking into account the solvation effect. The position of Rh-induces defect energy levels have been determined. Our findings indicated a substantial reduction in overpotential for the Rhodium-modified TiO_2 surface compared to the bare surface. The high overpotential on the bare $BaTiO_3$ surface suggests low OER efficiency, making Rh doping a promising strategy for enhancement.

1. Introduction

The growing demand for environmentally friendly and cost-effective sources of energy has led to intensive research into various renewable energy sources. In this regard, photoelectrochemical hydrogen generation through water splitting has emerged as a promising avenue due to its affordability and environmental friendliness. In 1972, Honda and Fujishima first reported the production of hydrogen through photochemical water splitting using the semiconductor TiO_2 [1]. Since then, this phenomenon has been extensively studied, leading to the development of numerous materials and water splitting systems. One of the most studied semiconductors includes materials based on TiO_2 and ferroelectric strontium titanate $SrTiO_3$ (STO) and barium titanate $BaTiO_3$ (BTO) [1–11]. Ferroelectrics have the advantage of spatially separating photogenerated charge carriers with a spontaneously polarized electric field. However, their main drawback is the wide bandgap, which is 3.2 eV for BTO [12] and 3.75 eV for STO [13]. This results in the predominant absorption of light in the ultraviolet range, significantly reducing the efficiency of solar radiation conversion. Additionally, both materials suffer from high rates of photoinduced charge recombination. Much of the research in this field is focused on increasing light absorption and suppressing charge recombination. When these issues are resolved, it is expected that hydrogen generation through water splitting using solar energy will become the most cost-effective method for hydrogen production [9]. Barium titanate is promising and low-cost material for hydrogen production in a photoelectrochemical cell. It has an appropriate band position for water splitting and pollutant degradation, as well as favorable chemical stability. Its unique optoelectronic, piezoelectric and ferroelectric properties are of great importance from a technological point of view [14]. Synthesis methods developed the specific shaped $BaTiO_3$ nanocrystals with the precisely controlled ratio of in-plane and out-of-plane domains. These nanocrystals are primarily [001]-oriented microscale and submicron plates, synthesized under optimized conditions [14]. These tailored $BaTiO_3$ plates enhance charge separation at the level of individual plates.

Depending on the temperature, barium titanate crystallizes into various structures at atmospheric pressure. High-symmetry cubic phase (*Pm3 m*) $BaTiO_3$ that is stable above 390 K with decreasing temperature undergoes to tetragonal symmetry (*P4mm*) at 300–320 K, then to orthorhombic symmetry *(Amm2)* at 250–280 K, and finally to rhombohedral symmetry (*R3m*) at 200–240 K [15,16]. Fig. 1a–d represent the basic unit cell structures of the four phases of $BaTiO_3$.

Electrocatalyst properties of the cubic and tetragonal phases have been extensively studied [17–20], much less is known about the orthorhombic and rhombohedral phases. Here, for the first time, the process of water splitting on a rhombohedral pure and rhodium doped (001) $BaTiO_3$ surface is presented, and is also studied in a wet surface. Also, for the first time, process of water splitting on BTO surface

This paper was presented at the 12th International Conference on Luminescent Detectors and Transformers of Ionizing Radiation (LUMDETR), June 16-21, 2024, Riga, Latvia.

* Corresponding author.
E-mail address: abuova_fu@enu.kz (F.U. Abuova).

https://doi.org/10.1016/j.omx.2024.100382
Received 18 October 2024; Received in revised form 14 November 2024; Accepted 20 November 2024
Available online 28 November 2024

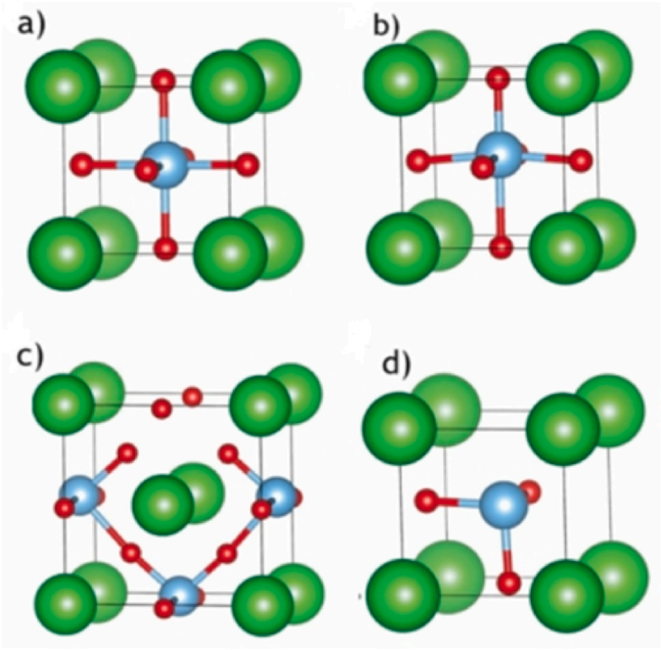

Fig. 1. 3D crystal structure of the unit cell of a) cubic, b)tetragonal, c) orthorhombic,
d) rhombohedral phase of $BaTiO_3$ polymorphs.

explained by means of DFT in atomistic scale.

Barium titanate, as an *n*-type semiconductor exhibits wide optical band gap about 3.2–3.4 eV [21], much larger than the termodynamical potential of 1.23 eV required for water splitting. In addition, due to the kinetic barriers of the termodynamics reactions, species of water splitting occurs at the potentials much larger than this value.

Several methods used for enhancing electronic properties of barium titanate for electrocatalysts application. Catalyst performance could be, in principle, improved using different promoters like W, Mn, Fe [22–24]. According to the theoretical study [17] Fe_{Ti}- and Ni_{Ti}-substituions increased electrical conductivity and reduced overpotentials for oxygen evolution reaction (OER). Xie et al. [25] revealed experimentally that at 2 % Mo – doping to BTO results in reduction of the optical bandgap for activation its photo-catalytic performance.

It has also been reported that anion mono- and co-doping of $BaTiO_3$ leads to modification of the geometrical crystal structure, energies of formation, electronic properties, and optical absorption characteristics [26]. Therefore, through the process of double-hole doping via anionic combinations, it becomes feasible to adjust the band structures of wide-band gap semiconductors, leading to the development of efficient catalysts for harnessing solar energy in water splitting applications.

Bhat [27] suggested that Rh-doped BTO resulted in a formation of mid gap states, causes to reduce the band gap of $BaTiO_3$ while simultaneously avoiding the formation of recombination centers. As seen from the above-mentioned studies, investigation of Rh modified impact to catalyst properties of BTO is limited and it requires more detail consideration. In this study we focus catalytic performance of pure and Rh modified rhombohedral BTO structure. In our previous studies [28], we focused on the tetragonal phase of barium titanate, as it is more stable at room temperature compared to other phases. Rhodium-doping to tetragonal phase BTO causes the material to absorb sunlight in almost the entire visible range and significantly reducing the overpotential values of the electrochemical reaction. In this work, we investigated the electronic structure and water splitting reaction on both Rh-doped and bare surface rhombohedral phase of barium titanate, determined to be the most energetically favorable structure based on our calculations.

2. Theoretical surface and termodynamic model

2.1. Thermodynamic description

Since the atomistic mechanism of the OER for BTO is complicated, insights into the thermodynamics of the reaction could be important, e. g. using the well-established approach developed by Norskov and co-workers [29,30].

The process of electrolysis of water to obtain hydrogen and oxygen is described succinctly:

$$H_2O = H_2 + \frac{1}{2}O_2$$

Or

$$H_2O + * \rightarrow *OH + H^+ + e^- \quad (1)$$

$$*OH \rightarrow *O + H^+ + e^- \quad (2)$$

$$*O + H_2O \rightarrow *OHH + H^+ + e^- \quad (3)$$

$$*OOH \rightarrow * + O_2 + H^* + e^- \quad (4)$$

where * means adsorbed particles or the surface itself. Or taking into account the cathode materials in this study:

$$Ba \rightarrow Ba^{2+} + 2e^-$$

$$Ba + H_2O \rightarrow Ba(OH)^+ + H^+ + 2e^-$$

$$Ba + 2H_2O \rightarrow BaO_2(s) + 4H^+ + 4e^-$$

$$Ti \rightarrow Ti^{2^+} + 2e^-$$

$$Ti + 2H_2O \rightarrow TiO_2^{2+} + 4H^+ + 6e^-$$

$$Ti + 2H_2O \rightarrow TiO_2(s) + 4H^+ + 4e^-$$

$$2H_2O + 2e^- \rightarrow 2OH^- + H_2(g)$$

$$\frac{1}{2}O_2(g) + 2H^+ + 2e^- \rightarrow H_2O$$

The spontaneous occurrence of this isobaric-isothermal process is described by the Gibbs free energy, which is determined by the enthalpy (ΔH) and entropy ($T\Delta$ S) factors:

$$\Delta G = \Delta H - T\Delta S \quad (5)$$

From (5) follows the thermal effect of the process:

$$\Delta H = \Delta G - T\Delta S$$

Therefore, $= \Delta G - T\Delta S$, that is, a certain amount of heat is spent to increase entropy, this part of the energy is lost to perform useful work (dissipated into the environment in the form of heat). The other part of the heat can be used to do the work. The enthalpy of the process (atomization energy, cohesive energy) of intermediate processes of water splitting on the surface of electrode materials from DFT calculations is equal to the adsorption energy:

$$\Delta E_{OH} = E(OH^*) - E(*) - \left[E(H_2O) - \frac{1}{2}E(H_2)\right]$$

$$\Delta E_0 = E(0^*) - E(*) - [E(H_2O) - E(H_2)]$$

$$\Delta E_{00H} = E(OOH^*) - E(*) - \left[2E(H_2O) - \frac{3}{2}E(H_2)\right]$$

Using the normal hydrogen electrode approach, the reaction free energy

ΔG of the charge transfer reaction $(*)H \rightarrow (*) + H^{2+} + e^{-}$ at standard ambient conditions can be related to the reaction

$AH(*)H \rightarrow (*) + 1/2H_2$. The reaction Gibbs free energies of the individual charge transfer steps, ΔG_1, ΔG_2, ΔG_3, and $\Delta G_4 E_{qs}$. (1–4) depend on the adsorption energies of OH^*, O*, and OOH^* and include zero point energy (ZPE) and entropy corrections [31]:

$$\Delta G_i = \Delta E_i - T\Delta S_i + \Delta ZPE_i - eU$$

Theoretical overpotential is calculated as:

$$\eta = \max[\Delta G_i]/e - 1,23(V)$$

2.2. Structure models

Rhombohedral $BaTiO_3$, stable phase of barium titanate stable in the lowest temperature below 90 °C and is ferroelectric. In high symmetry cube phase BTO Ba atoms are placed at the eighth apexes of the cube corner, Ti atoms occupy the center of the cube, and O atoms are located at the face centers, forming a symmetric octahedron (TiO_6). Optimization structure geometry calculations performed for four bulk phases of $BaTiO_3$ [32]. Calculated lattice parameters (*a, b, c*) (Å) and α in good agreement with the experimental results and values of other theoretical studies shown in (Table 1).

The lattice structure of rhombohedral phase is similar to cubic one with distortion of Ti, O from atomic positions in cubic structure. Titanium is displaced along the body diagonal from the center by - 0.0137 Å. All oxygen atoms are displaced in the opposite [111] direction along the body diagonal by about 0.0232 Å. Calculated bond lengths Ba–O (2.87 Å) and Ti–O (1.89 Å) are in a good agreement with the experimental measurements [35,36] and the values from the previous theoretical studies [37,38]. The calculated direct band gap for rhombohedral phase of 2.25 eV, shown in Fig. 2,is in good agreement with other theoretical data [34]. It is well known that the GGA-PBE underestimate the band gap similarly to other theoretical studies [27].

We use slab models in rhombohedral phase $BaTiO_3$ along the (001) crystallographic plane by replicating symmetrically with respect to the mirror plane slabs consisting of 7 alternating TiO_2- and BaO-planes with the vacuum gap of 13 Å. $BaTiO_3$ (001) surface is nonpolar.

The surface energy was calculated as:

$$\gamma = \frac{E_{slab} \; nE_{bulk}}{2mS} \quad (7)$$

where E_{slab} denotes the slab energy and nE_{bulk} energy of the corresponding number of $BaTiO_3$ units in the bulk, m is the number of elementary surface units s. Because the surface system is modeled by a slab with two equivalent surfaces, the surface free energy is divided by two.

3. Results and discussions

3.1. Rh doping on $BaTiO_3$ (001) surface

In our study, we investigated the catalytic performance of pure and Rh-doped TiO_2-terminated $BaTiO_3$ (001) surfaces, for H_2O adsorption. The properties of barium titanate for redox reactions can be enhanced by

Table 1
Calculated and experimental Lattice parameters (*a, b, c*) (Å), equilibrium volume V_0 ($Å^3$).

$BaTiO_3$ phases	Presentwork	Theoretical [33]	Theoretical [34]	Theoretical [35]
Rhombohedral	*a,b,c*(Å) V_0($Å^3$) $a = b = c =$ 4.073 67.613	*a, b, c* (Å) $a = b = c =$ 4.073	*a, b, c* (Å) $a = b = c =$ 4.053	*a, b, c* (Å) $a = b = c =$ 4.004

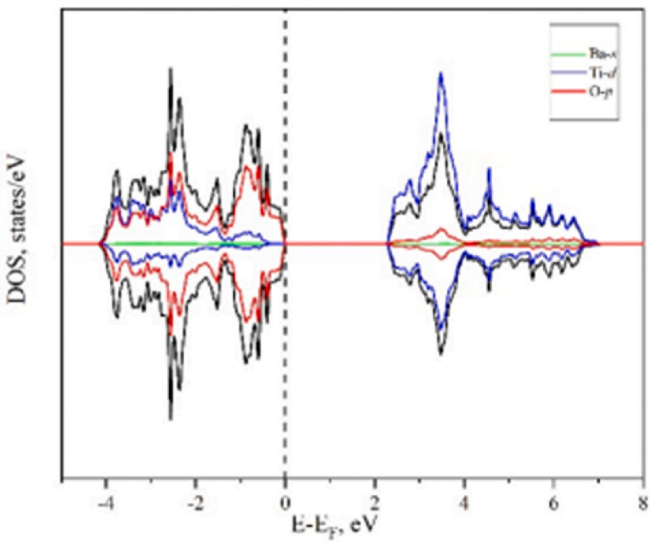

Fig. 2. The electronic DOS of a pure $BaTiO_3$.

introducing various dopants. To examine the impact of Rh doping, one, two, and three titanium atoms were replaced with rhodium ion on the $BaTiO_3$ (001) surfaces with TiO termination, as illustrated in Fig. 3.

The evaluation of the substitution energy of surface titanium ions with rhodium atoms on the plate's surface was performed using the following expressions:

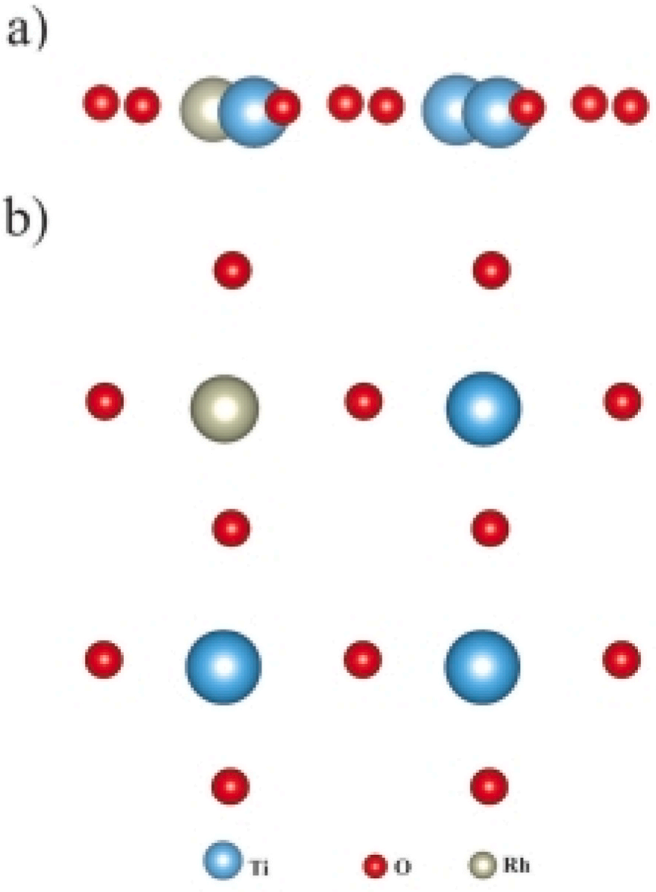

Fig. 3. Side (a) view and Top (b) view of rhodium doping of the TiO_2-terminated surfaces.

$$E_1 = E(BaTiO_3)_{perf} + E(Rh)_{peratom}$$

$$E_2 = E(BaTiO_3 + Rh_{Ti}) + E(Ti)_{peratom}$$

$$E_{Subtitution} = \frac{E_2 - E_1}{2} \quad (8)$$

where $E(BaTiO_3)_{perf}$ represents the perfect surface, $E(Rh)_{peratom}$, $E(Ti)_{peratom}$ are the energies of per atoms, and $E(BaTiO_3 + Rh_{Ti})$ is the total energy value of the rhodium-doped surface.

The surface concentration of Rh per TiO_2 surface unit is ¼. After Rh doping, the structures were re-optimized. Calculations do not predict significant lattice relaxation around the doped Rh ion: the change in the equilibrium bond length between O and catalytically active titanium Ti–O is greater than the Ti–Rh bond by only Δl = 0.0017 Å (Δl = 0.0021 Å), respectively.

The effective charge of the Rh ion was 1.66*e*, which is slightly less than the 2.55*e* charge of the Ba ion on TiO_2 termination. The Rh doping energy values, calculated using **Equation (8)**, for the (001) surface termination of TiO_2, along with the charges on the atoms, are shown in Table 2. The obtained E_{doping} values, using **Equation (8)**, is 7.72 *e*V for TiO_2 termination. The electronic structure of doped and undoped models is schematically presented in Fig. 3.

3.1.1. Density of states

The electronic configuration of titanium, oxygen, and rhodium is as follows: Ti = [Ar]$3d^2$ $4s^2$, O = [He]$2s^2$ $2p^4$и Rh = [Kr]$4d^8$ $5s^1$. The electronic structure of doped and undoped models is schematically presented in Fig. 4. Fig. 4a and b shows the influence of doping on the electronic properties of TiO_2- terminated slabs, and the calculated total and projected atomic orbital densities of states (DOS) are illustrated. Based on the calculated density of states, it can be observed that for the undoped model, all orbitals in the valence bands are composed of oxygen 2*p* orbitals, while all orbitals in the conduction band (CB) consist of titanium 3*d* orbitals. The density of states for the undoped model in Fig. 4a approximately reproduces the density of states for the doped model in Fig. 4b in the energy range below −1.5 *e*V (VB) and above approximately 1 *e*V (CB).

In experimental study [20], doping Rh species into the lattice of $BaTiO_3$ resulted in the formation of new absorption bands in visible light region. Absorption edge at around 500 nm assigned to Rh3+ species while another absorption band observed at 700 nm is attributable to Rh4+ species. With increasing the doping amount of Rh clearly observable cathodicphotoresponse in photocell confirms that $BaTiO_3$:Rh a stable p-type semiconductor for water reduction.In experimental study [39] Rh dopant lead to activation of visible light absorption up to 550 nm and an onset potential as high as 1.0 V. Revealed withphotovoltage spectroscopy the n-to p-type transition of the BTO was studied and explained microscopically by which we quantitatively isolated the cathodic contribution caused by the Rh dopant.As the dopantconsentration increased, the anodic photocurrent was suppressed, while cathodic photocurrents emerged concurrently.

Table 2
Basic characteristics of undoped and Rh-doped TiO_2 - terminated (001) $BaTiO_3$ surface.

TiO_2 - termination					
	E_{doped} (*e*V)	Distance (Å)	Atomiccharge (*e*)		
		O - Ba	O	Rh	Ba
Undoped	0	2.78	−1.42		1.53
Rh -doped	6.81	2.84	−1.34	1.12	1.56
BaO - termination					
	E_{doped} (*e*V)	Distance (Å)			
		O - Ti	O	Rh	Ti
Undoped	0	2,28	−1,33	–	2,55
Rh -doped	7,72	2,26	−1,21	1,66	2,50

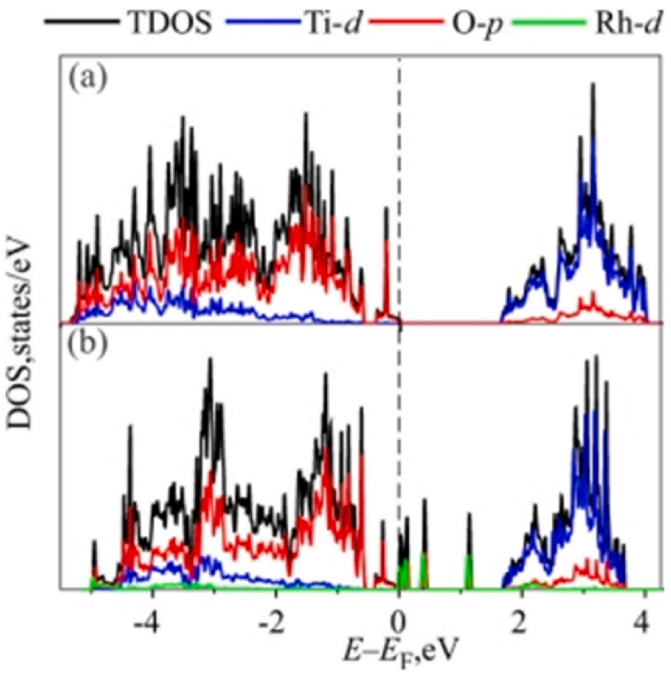

Fig. 4. Basic electronic structure features for the undoped (a) and doped (b) TiO_2 terminated (001) surface. Panels a, b show comparison of total density of states (lines) and partial density of states components on O 2*p* (red lines), Ti 3*d* (blue lines), and Rh 4*d* (green lines) for undoped and doped models. Undoped surface has a bandgap of over 1.65 *e*V. Doped surface shows states contributed by doping in the bandgap area. (For interpretation of the references to colour in this figure legend, the reader is referred to the Web version of this article.)

Considered photocatalytic activities of Rh modified rutile and anatase TiO_2 are strongly correlated with its crystal phases and gave similar results in our study [40]. It was revealed that Rh atom generates energy levels above the valence band of TiO_2 and reduces the bandgap. The distribution of density of states shows that defect states appear with Rh and O hybridized orbitals in the middle of the bandgap for both rutile and anatase TiO_2.

For Rh_{Ti}, we see that the electronic structure exhibits an in-bandgap acceptor level of 0.115 *e*V above the Fermi level, which reduces the bandgap level from 1.45 eV to 0.67 *e*V (Fig. 4b). The lifetime of photogenerated electrons and holes is greatly influenced by the presence of this acceptor level since it can act as a recombination center, where pDOS shows that the acceptor level is formed by the hybridization of *d*-orbitals of Rh and Ti atoms. The valence band edge is formed by the *d* orbitals of the Rh atom as well as the *p* orbitals of O atoms.

3.2. H_2O splitting on Rh-doped BaTiO3 (001) surface

It was previously shown that the TiO_2-terminated surface is stable under operating conditions. In contrast, the BaO-terminated surface is unstable concerning Ba dissolution at a wide range of pH values and potentials [39]. Based on these results, we evaluate the reaction-free energy profile for the OER on the TiO_2-terminated surface of $BaTiO_3$, as described in the methods section.

In this part, we investigated the splitting of H_2O on a pure and Rh-doped $BaTiO_3$ (001) surface, where the surface concentration of doped Rh was 1/4 per TiO2 surface unit.

The energy of adsorption was calculated:

$$\Delta E_{ads} = E_{adsorbate/surface} - \left(E_{adsorbate} + E_{surface}\right) \quad (9)$$

where $E_{adsorbate/surface}$, $E_{adsorbate}$ and $E_{surface}$ correspond to the total energies

of a system formed by the adsorbate at the surface, the isolated adsorbate in gas phase and the bare surface, respectively. Fig. 5 shows water adsorption geometries at the pristine $BaTiO_3$ (001) surface terminations.

Fig. 5 illustrate the geometry of water adsorption on Rh-doped $BaTiO_3$ (001) TiO_2-terminated surfaces. On the pure TiO_2-terminated surface, OOH particles adsorb with the energy of 3.43 eV (the distance Ti - O(H) is 2.65 Å), whereas at the Rh doping TiO_2 termination, OOH particles adsorb with the energy of 2.39 eV, and the distance Rh - O(H) is 1.92 Å. Considering the aqueous environment, this value is 3.51 eV. For the Rh-modified surface, the adsorption energy value is 2.21 eV, which is slightly different from a dry surface.

The binding energies of O, OH, and *OOH*($\Delta E_O \Delta E_{OH} \Delta E_{OOH}$ and bond lengths on the initial and Rh-doped TiO_2-terminated $BaTiO_3$ (001) surfaces are summarized in Table 3 display the charge values q of adsorbed elements on the pure and Rh-doped TiO_2-terminated (001) surfaces during the adsorption of O, OH, and OOH.

We have calculated the Gibbs free energy changes along the reaction pathway using the computational standard hydrogen electrode (SHE) allowing us to replace a proton and an electron with the half a hydrogen molecule at U = 0 V vs SHE according to theory [29,30]. The theoretical overpotential is found according to the standard relation

$$\eta = \max[\Delta G_i] / e - 1,23(V)$$

Fig. 6 present the free energy changes of reactions (1)–(4) based on DFT calculations of adsorbed intermediates on the undoped and Rh-doped $BaTiO_3$ (001) surface at ¼ *surface* concentration of dopant ions. The ideal potential is U = 1.23 V, and the responses in the equation are at U = 0. The oxidation reaction of a single water molecule is considered both on a dry surface and considering the influence of the aqueous environment. An H_2O molecule on a bare TiO_2-terminated surface was found to have an overpotential of 1.27 V when the surface is dry. This value is close to the earlier reported ones calculated on the TiO_2-terminated surfaces of tetragonal phase barium titanate [28,41]. In the case of aqueous environment, this value is reduced to 1.04 V similar to value on a wet surface which reviewed in recently study [28]. For the Rh-modified surface, the overpotential values are 0.12 V and 0.08 V for dry and wet surfaces, respectively.

For a more detailed understanding of the reasons for the reduced overpotential on the Rh-doped surface as well as on the undoped surfaces, Table 4 provides the redistribution of electron (Bader) charges on both sites, as well as on O, OH, OOH.

When the surface titanium ion is replaced with rhodium, the dopant

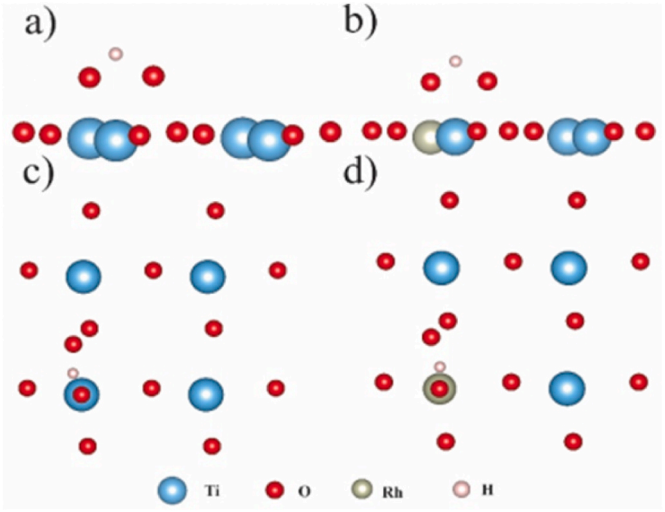

Fig. 5. a) Side view and (b) top view of water adsorption on pure TiO_2 -terminated surface. (c) Side view and (d) top view Rh-doped of water adsorption on TiO_2 -terminated surface.

Table 3
The binding energies of O, OH and OOH (ΔE_O, ΔE_{OH}, ΔE_{OOH} in eV) and bond length on the Rh-doped (001) TiO_2-terminated surface. d_x - is bond length in Å, * denotes adsorbate atom.

		ΔE_O	$d_{Rh\text{-}O}$	ΔE_{OH}	$d_{Rh\text{-}O(H)}$ $d_{O(*)\text{-}H(*)}$	ΔE_{OOH}	$d_{Rh\text{-}O}$ $d_{O(*)\text{-}H(*)}$ $d_{O(*)\text{-}O(*)}$
Dry	Undoped	4.12		1.30		4.40	
	Rh-doped	2.52	1.75	0.45	1.91 0.98	2.58	1.92 0.98 2.92
Wet	Undoped	4.34		4.01		7.58	
	Rh-doped	2.46	1.75	0.41	1.92 0.98	2.69	1.92 0.98 2.96

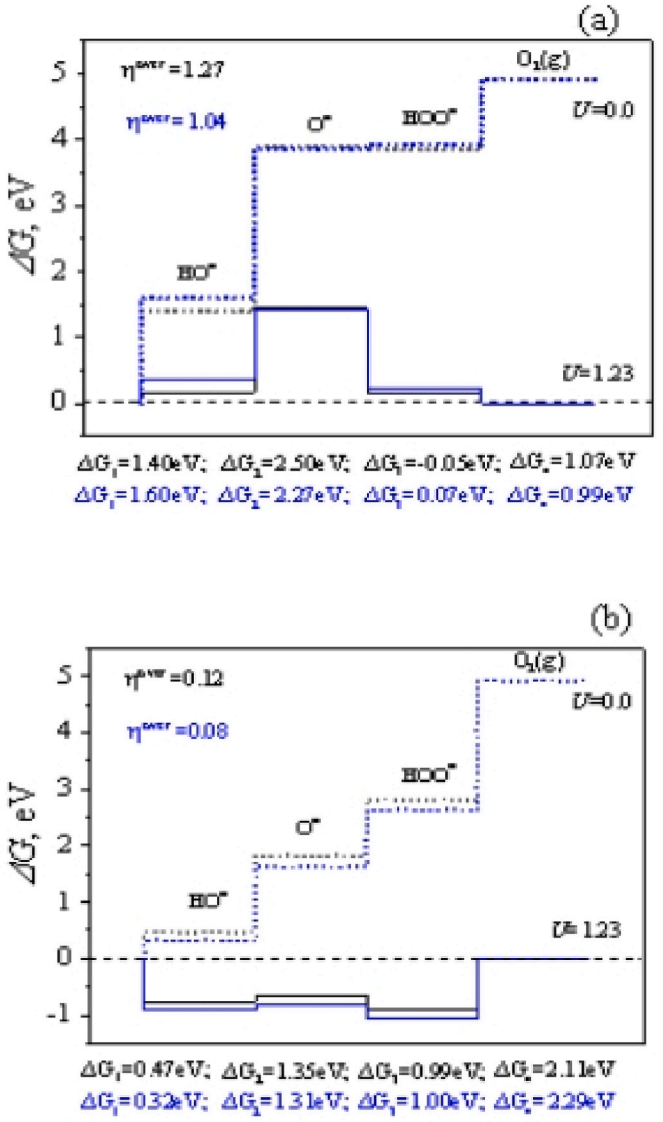

Fig. 6. Standard free energy diagram for the OER at zero potential (U = 0, dotted lines) and equilibrium potential for oxygen evolution (U = 1.23 V, solid lines) at pH = 0 and T = 298 K for the undoped (a) and doped (b) TiO_2 terminated (001) surface. Black and blue lines show data for dry and wet surfaces, respectively. Dashed lines correspond to the ideal catalyst. (For interpretation of the references to colour in this figure legend, the reader is referred to the Web version of this article.)

Table 4
TiO_2-terminated surface. Calculated Bader charges q(in |e|) and local magnetic moments (in μB) for the Ti (undoped surface) and Rh (doped surface) empty sites and as well as sites occupied by O, OH and OOH.

Undopedsurface									
		Emptysite (*)		OH*		O*		OOH*	
	Specie	**Q**	**μ**	**q**	**μ**	**Q**	**μ**	**q**	**μ**
Dry	Ti	2.17	0	2.24	0	2.22	0	2.16	0
	O1	−1.23	0	−1.25	0	−1.25	0	−1.27	0
	O2	−1.18	0	−1.18	0	−1.14	0	−1.18	0
	Adsorbant	–	–	−0.51	0	−0.52	0.36	−0.25	0.02
Wet	Ti	2.21	0	2.23	0	2.21	0	2.16	0
	O1	−1.24	0	−1.25	0	−1.21	0	−1.27	0
	O2	−1.20	0	−1.18	0	−1.15	0	−1.14	0
	Adsorbant	–	–	−0.56		−0.71	0.38	−0.29	0.04
Dopedsurface									
Dry	Rh	1.40	1.6	1.66	0.93	1.80	1.01	1.67	0.80
	O1	−1.15	0.16	−1.17	0.01	−1.17	0.02	−1.16	0.01
	O2	−1.11	0.04	−1.12	0.06	−1.08	0.03	−1.11	0.04
	Adsorbant	–	–	−0.30	1.04	−0.45	1.02	−0.19	0.31
Wet	Rh	1.45	1.61	1.66	0.94	1.77	1.03	1.66	0.82
	O1	−1.15	0.17	−1.17	0.02	−1.17	0.03	−1.16	0.01
	O2	−1.13	0.04	−1.06	0.06	−1.09	0.04	−1.10	0.04
	Adsorbant	–	–	−0.38	1.08	−0.59	1.04	−0.23	0.27

affects its neighboring O1 and O2 ions. As shown in Table 4, the absolute value of the Bader charge on O1 and O2 decreases, and a non-zero magnetic moment appears on these ions, indicating charge transfer from O1 and O2 to the dopant. The spin state of the Rh ion further indicates that it is not in the 4+ oxidation state, which would correspond to a formal magnetic moment of 1 μB in the low-spin state ($4d^5$). The current calculations suggest a spin magnetic moment of 1.66 μB for Rh, indicating it is in the 3+ oxidation state, with a formal magnetic moment of 2 μB in the intermediate spin state. This deviation from the formal value is due to charge transfer from O1 and O2 to the doping cation.

During water oxidation, the magnetic moment of Rh changes from 1.01 μB (O*) to 0.93 μB (OH*) and then to 0.80 μB (OOH*). This suggests that the oxidation state of Rh transitions from 3+ (O*) to 4+ (OH* and OOH*). As a result of the water oxidation reaction, the oxidation state and spin magnetic moment of ions on the catalyst surface, as well as the reaction intermediates, change. The ability of Rh and the surrounding ions on the surface to alter their electronic properties enhances water oxidation efficiency. Additionally, the aqueous environment significantly impacts the behavior of OH* species, leading to a decrease in overpotential. The water oxidation reaction causes changes in the oxidation state and spin magnetic moment of the ions on the catalyst surface, along with the reaction intermediates. The capacity of Rh and nearby surface ions to alter their electronic properties enhances water oxidation efficiency. The aqueous environment notably impacts the behavior ofOH* species, resulting in a reduction of the overpotential.

4. Methods

4.1. Computation details

Theoretical description of structural, optical and electronic properties performed with the *ab initio* plane wave computer code VASP [42,43] using the projector-augmented plane wave (PAW) formalism [44] in conjunction with PBE (Perdew – Burke– Ernzerhof) GGA exchange-correlation functional [45]. The thermodynamic corrections for the solvation effect were calculated using VASPsol [46]. Monkhorst–Pack grid sampling mesh for the bulk calculations was 2 × 2 × 2 and for the slab calculations 2 × 2 × 1 with the cutoff energy value of 520 eV. The convergence tolerance for the calculations was chosen as the difference in total energy within 10^{-6} eV. The following electronic configurations were used for pseudopotentials: Ba ($6s^2$), Ti ($3d^2$ $4s^2$), O ($2s^2$ $2p^4$), Rh ($4d^8$ $5s^1$). We simulated symmetric slabs with an odd number of layers, for which the total dipole moment is zero. As the number of slab layers exceeds eleven, the atomic relaxation and the surface energy finally converge. This slab is stoichiometric and symmetric along the surface normal plane.The charge distribution on the ions was studied using Bader topological analysis [47].

5. Conclusions

Using DFT calculations, we showed how the Gibbs free energy changes along the OER on pure and Rh-doped (001) $BaTiO_3$ surfaces. Changing the oxidation state of rhodium from 3+ to 4+ during the splitting water and adsorption of intermediate products the surface oxygen ions acquire a charge from the surface, this, in turn, increases the binding energy between surface ions and adsorbates. This reduces the bond energy between the adsorbate ions, resulting in a decrease in overpotential. The overpotential of the TiO_2 Rh-doped surface is significantly reduced compared to undoped surface. Due to the significant overpotential, the OER efficiency on undoped $BaTiO_3$ surface is expected to be low, and thus Rh doping effectively increases it. This means that Rh-doped $BaTiO_3$ is active in the electrochemical oxidation of water, which is in full agreement with experimental observations and previous studies [28,41].

CRediT authorship contribution statement

G.A. Kaptagay: Writing – original draft, Project administration, Methodology, Conceptualization. **B.M. Satanova:** Writing – original draft, Investigation, Conceptualization. **A.U. Abuova:** Software, Investigation, Formal analysis. **M. Konuhova:** Software, Methodology, Investigation. **Zh.Ye. Zakiyeva:** Data curation, Visualization. **U. Zh Tolegen:** Visualization, Data curation. **N.O. Koilyk:** Validation, Supervision, Formal analysis. **F.U. Abuova:** Writing – review & editing, Software, Investigation, Formal analysis, Conceptualization.

Authors agreement

Authors believe that this subject would attract scientists' attention and would facilitate healthy discussion in the community.

- We confirm that neither the manuscript nor any parts of its content are currently under consideration for publication with or published in another journal.

- All authors have approved the manuscript and agree with its submission to Optical Materials:X (LUMDETR 2024 Proceedings) journal.

Funding

"This work was supported by the Ministry of Science and Higher Education of the Republic of Kazakhstan, grant number IRN AP14972859".

Declaration of competing interest

The authors declare the following financial interests/personal relationships which may be considered as potential competing interests: Fatima Abuova, Kaptagay Gulbanu reports financial support was provided by Ministry of Science and Higher Education of the Republic of Kazakhstan. If there are other authors, they declare that they have no known competing financial interests or personal relationships that could have appeared to influence the work reported in this paper.

Data availability

Data will be made available on request.

References

[1] A. Fujishima, K. Honda, Electrochemical photolysis of water at a semiconductor electrode, Nature 238 (5358) (1972) 37–38, https://doi.org/10.1038/238037a0.
[2] H. Kato, A. Kudo, Visible-light-Response and photocatalytic activities of TiO_2 and $SrTiO_3$Photocatalysts Co doped with antimony and chromium, J. Phys. Chem. B 106 (2002) 5029–5034, https://doi.org/10.1021/jp0255482.
[3] R. Konta, T. Ishii, H. Kato, A. Kudo, Photocatalytic activities of noble metal ion doped $SrTiO_3$ under visible light irradiation, J. Phys. Chem. B 108 (2004) 8992–8995, https://doi.org/10.1021/jp049556p.
[4] R.I. Eglitis, A.I. Popov, J. Purans, D. Bocharov, Y. Mastrikov, R. Jia, S.P. Kruchinin, Ab initio computations of$BaZrO_3$, $CaTiO_3$, $SrTiO_3$ perovskite as well as $WO_3$and ReO_3 (001)surfaces, Low Temp. Phys. 48 (10) (2022) 811–818, https://doi.org/10.1063/10.0014024, 2022.
[5] Y. Ham, T. Hisatomi, Y. Goto, Y. Moriya, Y. Sakata, A. Yamakata, J. Kubota, K. Domen, Flux-mediated doping of $SrTiO_3$photocatalysts for efficient overall water splitting, J. Mater. Chem. A 4 (2016) 3027–3033, https://doi.org/10.1039/C5TA04843E.
[6] T. Kanazawa, S. Nozawa, D. Lu, K. Maeda, Structure and photocatalytic activity of $PdCrO_x$Cocatalyst on $SrTiO_3$ for overall water splitting, Catalysts 9 (2019), https://doi.org/10.3390/catal9010059, 59-11.
[7] R.I. Eglitis, S. Piskunov, A.I. Popov, J. Purans, D. Bocharov, R. Jia, Systematic trends in hybrid-DFT computations of BaTiO3/SrTiO3,PbTiO3/SrTiO3 and PbZrO3/SrZrO3 (001) hetero structures, Condens. Matter. 7 (2022), https://doi.org/10.3390/condmat7040070, 70-20.
[8] C. Yang, Y. Chen, T. Chen, S. Rajendran, Z. Zeng, J. Qin, X. Zhang, A long-standing polarized electric field in TiO_2@$BaTiO_3$/CdS nanocomposite for effective photocatalytic hydrogen evolution, Fuel 314 (2022), https://doi.org/10.1016/j.fuel.2018.04.300, 122758-11.
[9] P. Xie, F. Yang, R. Li, C. Ai, C. Lin, S. Lin, Improving hydrogen evolution activity of perovskite $BaTiO_3$ with Mo doping: experiments and first-principles analysis, Int. J. Hydrogen Energy 44 (2019) 11695–11704, https://doi.org/10.1016/j.ijhydene.2019.03.145.
[10] H.-C. Huang, C.-L. Yang, M.-S. Wang, X.-G. Ma, Chalcogens doped BaTiO3 for visible light photocatalytic hydrogen production from water splitting, Spectrochim. Acta Part A Molecular and Biomolecular Spectroscopy 208 (2019) 65–72, https://doi.org/10.1016/j.saa.2018.09.048.
[11] R.I. Eglitis, J. Purans, A.I. Popov, D. Bocharov, A. Chekhovska, R. Jia, Ab initio computations of O and AO as well as ReO_2, WO_2 andBO_2-terminated ReO_3, WO_3, $BaTiO_3$, $SrTiO_3$ and $BaZrO_3$ (001) surfaces, Symmetry 14 (2022), https://doi.org/10.3390/sym14051050, 1050-16.
[12] S.H. Wemple, Polarization fluctuations and the optical-absorption edge in $BaTiO_3$, Phys. Rev. B 2 (1970), https://doi.org/10.1103/PhysRevB.2.2679, 2679-5.
[13] K. Van Benthem, C. Elsässerand, R. French, Bulk electronic structure of $SrTiO_3$: experiment and theory, J. Appl. Phys. 90 (2001), https://doi.org/10.1063/1.1415766, 6156-12.
[14] M.M. Kržmanc, B. Jančar, H. Uršič, M. Tramšekand D. Suvorov, Tailoring the shape, size, crystal structure, and preferential growth orientation of $BaTiO_3$ plates synthesized through a topochemical conversion process, J.Crystal Growth & Design 6 (17) (2017) 3210–3215, https://doi.org/10.1021/acs.cgd.7b00164.
[15] U. Chon, et al., Layered perovskites with giant spontaneous polarizations for nonvolatile memories, Phys. Rev. Lett. 8 (89) (2002), https://doi.org/10.1103/PhysRevLett.89.087601, 087601-5.
[16] R. Waser, in: Nanoelectronics and Information Technology: Advanced Electronic Materials and Novel Devices, third ed., 2012.
[17] P. Qin, H. Song, Q. Ruan, Zh, Huang, Y. Xu, C. Huang, Direct observation of dynamic surface reconstruction and active phases on honeycomb Ni3N–Co3N/CC for oxygen evolution reaction, Sci. China Mater. 65 (9) (2022) 2445–2446, https://doi.org/10.1007/s40843-021-1995-4.
[18] Y. Zhang, H. Khanpureh, S. Dunn, C. R. Bowen, H. Gong, N. P. H. Duy and P. T. Phuong, High Efficiency Water Splitting using Ultrasound Coupled to a BaTiO3 Nanofluid, Adv. Sci., 9(9) 1 (2022)2105248-11.https://doi.org/10.1002/advs.202105248.
[19] O. Küçük, S. Teber, I.C. Kaya, H. Akyıldız, V. Kalem, Photocatalytic activity and dielectric properties of hydrothermally derived tetragonal BaTiO3 nanoparticles using TiO_2 nanofibers, J. Alloys Compd. 765 (2018), https://doi.org/10.1016/j.jallcom.2018.06.165, 82-12.
[20] K. Maeda, Rhodium-doped barium titanate perovskite as a stable p-type semiconductor photocatalyst for hydrogen evolution under visible light, ACS Appl. Mater. Interfaces 6 (3) (2014), https://doi.org/10.1021/am405293e, 2167-7.
[21] S.H. Wemple, Perovskite-type $SrTiO_3$, $CaTiO_3$ and $BaTiO_3$ porous film electrodes for dye-sensitized solar cells, Phys. Rev. B 2 (1970), https://doi.org/10.1021/PR181545i, 2679-5.
[22] S. Upadhyay, J. Shrivastava, A. Solanki, S. Choudhary, V. Sharma, P. Kumar, N. Singh, V.R. Satsangi, R. Shrivastavand, U.V. Waghmare, et al., Enhanced photoelectrochemical response of BaTiO3 with Fe doping: experiments and first-principles analysis, J. Phys. Chem. C 115 (2011) 24373–24380, https://doi.org/10.1021/jp202863a.
[23] M. Nageri, V. Kumar, Manganese-doped $BaTiO_3$ nanotube arrays for enhanced visible light photocatalytic applications, Mater. Chem. Phys. 213 (2018) 400–416, https://doi.org/10.1016/j.matchemphys.2018.04.003.
[24] P. Demirciviand, E.B. Simsek, Visible-light-enhanced photoactivity of perovskite-type W-doped $BaTiO_3$photocatalyst for photodegradation of tetracycline, J. Alloys Compd. (2019) 774–795, https://doi.org/10.1016/j.jallcom.2018.09.354.
[25] P. Xie, F. Yang, R. Li, C. Ai, C. Lin, S. Lin, Improving hydrogen evolution activity of perovskite BaTiO3 with Mo doping: experiments and first-principles analysis, Int. J. Hydrogen Energy 44 (2019) 11695–11704, https://doi.org/10.1016/j.ijhydene.2019.03.1.5.
[26] G.-S. Souraya, B.K. Mohammed, Insight into the effect of anionic–anionic Co-doping on $BaTiO_3$ for visible light photocatalytic water splitting: a first-principles hybrid computational study, Catalysts 12 (2022) 1672–1678, https://doi.org/10.3390/catal12121672.
[27] D.K. Bhat, H. Bantawal, U SShenoyRhodium doping augments photocatalytic activity of barium titanate: effect of electronic structure engineering, Nanoscale Adv. 2 (12) (2020), https://doi.org/10.1039/D0NA00702A, 5688-7.
[28] T. Inerbaev, A. Abuova, Zh Zakiyeva, F. Abuova, Y. Mastrikov, M. Sokolov, D. Gryaznov, E. Kotomin, Effect of Rh doping on optical absorption and oxygen evolution reaction activity on BaTiO3 (001), Molecules 29 (11) (2024) 2707–2715, https://doi.org/10.3390/molecules29112707.
[29] I.C. Man, H.-Y. Su, F. Calle-Vallejo, H.A. Hansen, J.I. Martínez, N.G. Inoglu, T. F. Kitchin, J.K. Jaramillo, J.K. Nørskov, J. Rossmeisl, Universality in oxygen evolution electrocatalysis on oxide surfaces, J. ChemCatChem. 3 (2010) 1159–1165, https://doi.org/10.1002/cctc.201000397.
[30] M. Garcia-Mota, M. Bajdich, V. Viswanathan, A. Vojvodic, A.T. Bell, J.K. Norskov, K. Jens, Importance of correlation in determining electrocatalytic oxygen evolution activity on cobalt oxides, J. Phys. Chem. C 116 (2012) 21077, https://doi.org/10.1021/jp306303y.
[31] W.M. Haynes, CRC Handbook of Chemistry and Physics, 93rd Edition, Taylor & Francis, 2000.
[32] T. Inerbaev, Zh Zakiyeva, F. Abuova, A. Abuova, S. Nurkenov, G. Kaptagay, DFT studies of $BaTiO_3$, Bulletin of the Karaganda University Physics Series 2 (2023) 72–78, https://doi.org/10.31489/2023PH2/72-78, 110.
[33] R.A. Evarestov, A. Bandura, V First-principles calculations on the four phases of $BaTiO_3$, J. Comput. Chem. (33) (2012) 1123, https://doi.org/10.1002/jcc.22942.
[34] H.-Y. Zhang, Z.-Y. Zeng, Y.-Q. Zhao, Q.Y. Lu, Z. Cheng, First-principles study of lattice dynamics, structural phase transition, and thermodynamic properties of barium titanate, Naturforscher 71 (2016), https://doi.org/10.1002/NF.201000397, 759-7.
[35] G.H. Kwei, A.C. Lawson, S.J.L. Billinge, Structures of the ferroelectric phases of barium titanate, J. Phys. Chem. (97) (1993), https://doi.org/10.1021/J100112A043, 2368-8.
[36] B. Ravel, E.A. Stern E A, R.I. Vedrinskii, V. Kraizman, Local structure and the phase transitions of $BaTiO_3$, Ferroelectrics 206 (1998) 407–430, https://doi.org/10.1080/00150199808009173.
[37] R. Eglitis, J. Purans, A.I. Popov, R. Jia, Systematic trends in $YAlO_3$, $SrTiO_3$, $BaTiO_3$, $BaZrO_3$ (001) and (111) surface ab initio calculations, Int. J. Mod. Phys. B 33 (32) (2019) 1950390, https://doi.org/10.1080/00150199908007992.
[38] A. Chakraborty, M.N.H. Liton, M.S.I. Sarker, M.M. Rahman, M.K.R. Khan, A comprehensive DFT evaluation of catalytic and optoelectronic properties of BaTiO3 polymorphs, Physica B: Phys. Condens. Matter 648 (2023), https://doi.org/10.1016/j.physb.2022.414418, 414418-11.
[39] K. Shi, B. Zhang, K. Liu, J. Zhang, G. Ma, Rhodium-doped barium titanate perovskite as a stable p-type photocathode in solar water splitting, ACS Appl. Mater. Interfaces 15 (2023) 47754–47758, https://doi.org/10.1021/acsami.3c09635.
[40] J. Wang, K. Liu, B. Zhang, Y. Qiu, Y. Xiang, W. Lin, B. Yang, B. Li, G. Ma, Doping Rh into TiO_2 as a visible-light-responsive photocatalyst: the difference between rutile and anatase, Appl. Phys. Lett. 119 (2021) 213901–213908, https://doi.org/10.1063/5.0070523.

[41] N. Artrith, et al., Reduced overpotentials for electrocatalytic water splitting over Fe- and Ni-modified $BaTiO_3$, 2Physical Chemistry Chemical Physics 18 (42) (2016) 29561–29565, https://doi.org/10.1039/c6cp06031e.
[42] G. Kresseand D. Joubert, Fromultrasoft pseudopotentials to the projector augmented-wave method, Phys. Rev. B 59 (3) (1999) 1758, https://doi.org/10.1103/PhysRevB.59.1758.
[43] G. Kresse, J. Furthmülle, Efficient iterative schemes for ab initio total-energy calculations using a plane-wave basis set, Phys. Rev. B 54 (16) (1996), https://doi.org/10.1103/PhysRevB.54.11169, 11169-12.
[44] P.E. Blöchl, Projector augmented-wave method, Phys. Rev. B 50 (24) (1994), https://doi.org/10.1103/PhysRevB.50.17953, 17953-12.
[45] J.P. Perdew, K. Burke, M. Ernzerhof, Generalized gradient approximation made simple, Phys. Rev. Lett. 77 (18) (1996) 3865–3866, https://doi.org/10.1103/PhysRevLett.77.3865.
[46] K. Mathew, R. Sundararaman, K. Letchworth-Weaver, T.A. Arias, R.G. Hennig, Implicit solvation model for density-functional study of nanocrystal surfaces and reaction pathways, J. Chem. Phys. 140 (2014), https://doi.org/10.1063/1.4865107, 084106-5.
[47] R. Bader, RFW atoms in molecules, Chem. Rev. V 893 (b) (1991) A, https://doi.org/10.1093/oso/9780198551683.001.0001. Quantum Theory.